Regulated spatial organization and sensitivity of cytosolic protein oxidation in Caenorhabditis elegans

Published in final edited form as:
Nat Commun. ; 5: 5020. doi:10.1038/ncomms6020.

Regulated spatial organization and sensitivity of cytosolic protein oxidation in *Caenorhabditis elegans*

Catalina Romero-Aristizabal[1], **Debora S. Marks**[1], **Walter Fontana**[1,*], and **Javier Apfeld**[1,*]
[1]Department of Systems Biology, Harvard Medical School, Boston, MA 02115, USA

Abstract

Cells adjust their behavior in response to redox events by regulating protein activity through the reversible formation of disulfide bridges between cysteine thiols. However, the spatial and temporal control of these modifications remains poorly understood in multicellular organisms. Here, we measured the protein thiol-disulfide balance in live *C. elegans* using a genetically-encoded redox sensor and found that it is specific to tissues and patterned spatially within a tissue. Insulin signaling regulates the sensor's oxidation at both of these levels. Unexpectedly, we found that isogenic individuals exhibit large differences in the sensor's thiol-disulfide balance. This variation contrasts with the general view that glutathione acts as the main cellular redox buffer. Indeed, our work suggests that glutathione converts small changes in its oxidation level into large changes in its redox potential. We therefore propose that glutathione facilitates the sensitive control of the thioldisulfide balance of target proteins in response to cellular redox events.

INTRODUCTION

The reversible formation of disulfide bonds between cysteine residues is increasingly recognized as an important mechanism for the regulation of protein function. These post-translational modifications can modulate the activity of a wide range of proteins, including transcription factors, kinases, metabolic enzymes and membrane channels[1, 2, 3, 4, 5, 6, 7]. As a result, these modifications affect diverse cellular processes, including metabolism, gene expression and cytoskeletal dynamics[7, 8]. A better understanding of the mechanisms that control these post-translational modifications *in vivo* may help to explain why the dysregulation of protein oxidation is a common factor in the development of many chronic diseases including diabetes, cardiovascular disease, neurodegenerative diseases and cancers[9, 10, 11, 12].

Organisms ranging from bacteria to humans control the formation of protein disulfides in the cytosol through the action of the glutathione and thioredoxin redox systems[13, 14].

Correspondence and requests for materials should be addressed to W.F. (walter@hms.harvard.edu) or J.A. (javier_apfeld@hms.harvard.edu).
*These authors are co-last authors.

AUTHOR CONTRIBUTIONS C.R. and J.A. conceived, designed and performed experiments, and analyzed data.
D.S.M. generated roGFP1_R12 vector.
J.A. and W.F. provided guidance.
C.R., J.A. and W.F. interpreted results and wrote the manuscript.

COMPETING FINANCIAL INTERESTS The authors declare that no competing interests exist.

Glutathione (GSH) reduces protein disulfides in a reaction that produces glutathione disulfide (GSSG). Similarly, thioredoxin (trx_{red}) reduces protein disulfides, in a reaction that produces oxidized thioredoxin (trx_{ox}). GSSG and trx_{ox} are reduced by NADPH in reactions catalyzed by specific enzymes[13]. As a result, the GSH/GSSG and trx_{red}/trx_{ox} couples act as shuttles of electrons between NADPH and protein disulfides[13].

The glutathione and thioredoxin couples have a broad spectrum of distinct but overlapping sets of target proteins[14]. Both of these couples can affect the formation of disulfides within and between proteins. In addition, the glutathione couple also affects the formation of disulfides between proteins and glutathione, which are known to modify the activities of a large number of proteins[9, 10, 11, 12]. The tendencies of the glutathione and thioredoxin couples to donate electrons to their target proteins are quantified by their redox potentials. Cellular inputs that affect the relative concentrations of these couple's oxidized and reduced species will shift their redox potential and tilt the thiol-disulfide balance of their respective protein targets. Thus, knowing the redox potential of these couples can inform us about the thiol-disulfide balance of the network of proteins they control[15].

The human and *C. elegans* proteomes contain approximately 210,000 cysteine residues, many of which can form disulfides[15, 16]. The regulation of protein oxidation under the control of the glutathione couple has remained largely unexplored in multicellular organisms due to the limitations of biochemical approaches that generally do not allow to differentiate between cellular compartments, tissues and even individuals[17]. The recent development of genetically-encoded fluorescent redox sensors that respond to the glutathione couple[17, 18, 19, 20, 21] has enabled studies of the *in vivo* distribution of this redox potential across sub-cellular compartments in plants[18, 19] and across tissues in fruit fly larvae[22]. Here, we used this approach to visualize the spatial organization of the glutathione redox potential in the cytosol of live *C. elegans* and quantify its sensitivity and dynamic response. We found that this redox potential is structured at the tissue and sub-tissue levels, and is regulated by insulin signaling at both of these levels. Notably, our work suggests that glutathione is not positioned to act as a buffer in the cytosol, since its redox potential is highly sensitive even to small changes in glutathione oxidation. This sensitivity may enable cells to respond to small perturbations of their cytosolic redox environment by adjusting the thiol-disulfide balance of the network of proteins controlled by the glutathione couple.

RESULTS

Measurement of protein oxidation *in vivo*

To visualize protein disulfide levels with spatial and temporal resolution in live *C. elegans* we used the redox probe roGFP1_R12, roGFP or “sensor” for short[23]. This sensor includes two cysteines whose thiol groups can form a reversible intramolecular disulfide bond. This oxidative modification changes the excitation profile of the sensor's chromophore by increasing absorption at the 410 nm excitation band and decreasing absorption at the 470 nm band[23, 24]. The resulting spectral changes allowed us to monitor the balance between reduced ($roGFP_{red}$) and oxidized ($roGFP_{ox}$) forms of the sensor via ratiometric fluorescence microscopy[24].

We first characterized the response of the sensor in live *C. elegans* upon exposure to exogenous oxidants and reductants that react directly with protein thiols. We treated animals expressing this sensor in the pharyngeal muscles with 50 mM diamide (a thiol-specific oxidant)[25] and then 100 mM dithiothreitol (DTT, a reducing agent), and observed the effect of this treatment time-course on the sensor's fluorescence (Fig. 1a–d). Diamide and DTT caused reciprocal changes in fluorescence, indicating that the sensor responds to oxidation and reduction reversibly (Fig. 1c,d). This treatment sequence resulted in the maximal oxidation and reduction of the sensor (see Methods). The resulting fluorescence ratio $R_{410/470}$ exhibited a large, 7.8 fold, dynamic range (Fig. 1b).

While $R_{410/470}$ values provide some information about the balance between oxidized and reduced forms of the sensor, they do not represent a biophysically interpretable magnitude. We derived the fraction of sensor molecules with a disulfide bond—OxD_{roGFP}, equal to $[roGFP_{ox}] / ([roGFP_{ox}] + [roGFP_{red}])$—by determining the three conversion parameters relating OxD_{roGFP} and $R_{410/470}$ from the fluorescence time-courses in diamide and DTT-treated animals (see Fig. 1e legend and Methods for details). The tendency of $roGFP_{ox}$ to acquire electrons and thereby become reduced into $roGFP_{red}$ is quantified by the half-cell reduction potential of the $roGFP_{red}/roGFP_{ox}$ couple, E_{roGFP}. This redox potential is given by the Nernst equation $E_{roGFP} = E^{\circ\prime}_{roGFP} - [RT/(2F)] \ln ([roGFP_{red}] / [roGFP_{ox}])$; where R is the gas constant, F the Faraday constant, T the absolute temperature, and $E^{\circ\prime}_{roGFP}$ the standard roGFP1_R12 midpoint potential, which is −265 mV (ref. [23]). Knowing OxD_{roGFP} made it possible to calculate E_{roGFP} by substituting in the Nernst equation the term $[roGFP_{red}] / [roGFP_{ox}]$ with the term $(1 - OxD_{roGFP}) / OxD_{roGFP}$, leading to the relation $E_{roGFP} = E^{\circ\prime}_{roGFP} - [RT/(2F)] \ln [(1 - OxD_{roGFP}) / OxD_{roGFP}]$ (Fig. 1e,f).

Previous studies demonstrate that roGFP-based sensors respond to the glutathione couple via glutaredoxin (see Supplementary Note 1). We measured the kinetics of spontaneous recovery from maximal oxidation by transferring animals from diamide treatment back to normal conditions. These *in vivo* reduction kinetics are fast (Supplementary Fig. 1, $t_{1/2}$ = 4.1 minutes), and are comparable to those observed *in vitro* in the presence of glutaredoxin[18, 19, 21]. This suggests that the endogenous levels of glutaredoxin are sufficient to ensure the equilibration of the sensor and glutathione couples in pharyngeal muscle. It is noteworthy that the fraction oxidized of roGFP1_R12 and, consequently, the associated redox potential of the sensor couple, are in a steady state in untreated animals (Supplementary Fig. 1,2), and reach a new steady state close to the original, upon recovery from diamide (Supplementary Fig. 1). The fast kinetics of reduction of the sensor, together with the observed stability in the sensor's redox potential over time, suggest that the sensor oxidation is in steady state in unperturbed animals because the redox environment controlling its oxidation is stable.

To determine whether the sensor responds to changes in the total amount of glutathione in live *C. elegans*, we measured its redox potential in feeding muscles of animals with reduced *gcs-1* activity. The *gcs-1* gene encodes the only glutamate-cysteine ligase in the genome, which catalyzes the rate-limiting first step in glutathione biosynthesis[26]. Animals with reduced *gcs-1* activity exhibit lower GSH levels than wild type[26]. The *gcs-1(ok436)* null allele causes larval lethality, so we examined young (L2) larvae lacking zygotic *gcs-1*

derived from *gcs-1* heterozygous parents. We found that the sensor's redox potential was significantly higher in *gcs-1(maternal+ zygotic−)* animals than in their *gcs-1(maternal+ zygotic+)* siblings (Supplementary Fig. 3). We conclude that roGFP1_R12 responds to changes in glutathione synthesis in live *C. elegans*.

The sensor's redox potential varies between tissues

To investigate the control of the sensor's redox potential across tissues of a live animal, we expressed the sensor in the cytosol of cells representing the three primary tissue layers: endoderm (intestine), mesoderm (pharyngeal muscles) and ectoderm (PLM neurons). Unexpectedly, we found that the sensor's redox potential in each of these tissues varied widely across individuals—up to 13 mV—even though these animals were genetically identical, had the same age and were cultured in the same environment. Despite this individual variation, the sensor's redox potential differed significantly between these three tissues (Fig. 2 and Supplementary Fig. 4). The intestine had the most oxidizing average redox potential (E_{roGFP} = −268.1 ± 2.1 mV), followed by the PLM neurons (E_{roGFP} = −269.9 ± 1.3 mV) and the pharyngeal muscles (E_{roGFP} = −270.9 ± 1.7 mV). We conclude that the sensor's redox potential is tissue specific.

The sensor's redox potential is patterned in the pharynx

To investigate the spatial control of the sensor's redox potential within a tissue of a live animal, we chose to focus on the pharynx, the feeding organ of *C. elegans* (Fig. 3a). This large organ has a simple and stereotyped anatomy that facilitates cellular identification. The pharynx is composed of eight adjacent muscles, pm1-pm8, aligned sequentially and connected by gap junctions[27]. We acquired profiles of the sensor's redox potential along the anterior-posterior (A-P) axis of the pharynx for 394 individuals. We found that these profiles vary considerably across individuals, even though these animals were genetically identical and were cultured in the same environment. At every position along the A-P axis, we observed substantial variation in the sensor's redox potential between individuals—up to 12 mV (Fig. 3b). Within an individual, the sensor's redox potentials in pm3, pm4, pm5, and pm7 muscles were strongly correlated (Supplementary Fig. 5). Therefore, the sensor's redox potential varies in a concerted manner throughout the pharynx.

Surprisingly, we found that the sensor's redox potential is not uniform throughout the anterior-posterior axis of the pharynx but, instead, is spatially patterned (Fig. 3c). We observed three distinct redox regions that align sharply with muscle boundaries (Supplementary Fig. 6a,b and Supplementary Movie 1). These redox regions may encompass multiple muscles, since pm3 and pm4 exhibit no significant difference in the sensor's redox potential (Supplementary Fig. 6). Along the A-P axis of the pharynx, sensor redox potentials are typically ordered: pm3 = pm4 < pm5 < pm7 (Fig. 3c and Supplementary Fig. 6). Differences between pairs of muscles vary widely between individuals—up to 7.5 mV (Supplementary Fig. 6c,d and Supplementary Movie 2). The redox potential difference between pm3 and pm5 is independent of the difference between pm5 and pm7 (Supplementary Fig. 7), indicating that the redox pattern is generated by two distinct mechanisms. We conclude that the pharyngeal redox profile is patterned by independent

mechanisms causing local deviations from the overall glutathione redox potential of the pharynx.

Insulin signaling regulates the sensor's redox potential

The well-defined redox pattern we observed in the pharynx and the redox-potential differences we observed across tissues suggest that the sensor's redox potential may be regulated at the tissue and sub-tissue levels. Insulin signaling has evolutionarily conserved effects on survival under oxidative stress[28, 29] making it a good candidate for the modulation of the sensor's redox potential. We examined mutants of *daf-2*, the only insulin receptor gene in *C. elegans*[30], and found that they exhibit a more reducing environment in the pharynx. The *daf-2(e1370)* mutation, which affects the kinase domain of the protein, and the *daf-2(m579)* mutation, which affects the ligand-binding domain and is homologous to the human type-A insulin resistance mutation[31], lower the sensor's redox potential by an average of 2.8 mV (Fig. 4a, Supplementary Fig. 8). We observed similar changes in the intestine of *daf-2(e1370)* mutants (Fig. 4b), but this mutation had no effect on redox potential in the cytosol of PLM neurons (Fig. 4c). Thus, under normal conditions, the effect of *daf-2* on redox potential is tissue specific.

Next, we determined whether insulin signaling regulates the spatial redox pattern of the pharynx. We acquired A-P profiles of the sensor's redox potential in mutants of the FOXO transcription factor DAF-16 whose activity is negatively modulated by signaling through DAF-2[32, 33]. We found that *daf-16(mu86)* null mutants exhibit higher redox potentials in the anterior muscles pm3 and pm5 than wild-type animals (Fig. 4d, Supplementary Fig. 9a). However, this mutation does not affect the sensor's redox potential in the posterior muscle pm7 (Fig. 4d and Supplementary Fig. 9a). Thus, in wild-type animals, DAF-16 is partially enabled in the anterior muscles of the pharynx and effectively switched off in the posterior. We also found that *daf-2(e1370)* lowers the sensor's redox potential at all positions along the pharyngeal A-P axis (Fig. 4d, Supplementary Fig. 9a). This effect is mediated by *daf-16*, since the redox profiles of the *daf-16* single mutants and *daf-16; daf-2* double mutants are indistinguishable (Fig. 4d,Supplementary Fig. 9a). We conclude that, in contrast to the wild-type case, DAF-16 is enabled in all positions along the A-P axis of the pharynx in *daf-2(e1370)* mutants. We quantified the relative magnitude of the genetic interaction between *daf-2* and *daf-16* in the control of the spatial variation of redox potential along the pharyngeal A-P axis using a functional version of categorical regression on genotype[34] (Fig. 4e). This analysis indicates that the quantitative regulation of DAF-16 by DAF-2 contributes to the redox pattern of the pharynx.

Glutathione does not act as a redox buffer in the cytosol

As we noted above, the fast kinetics of reduction and the stability of the sensor's redox potential, indicate that this potential equals the redox potential E_{GSH} of the cytosolic glutathione couple, under unperturbed conditions (Supplementary Fig. 1,2, Supplementary Note 1). Glutathione is the most abundant cellular thiol and is widely considered to act as the main redox buffer of the cell[1, 35, 36]. Based on this framework, we were surprised to observe a large E_{GSH} variation between individuals (Fig. 2b, 3b), since this variation is likely to cause significant differences in the thiol-disulfide balance of proteins targeted by

the glutathione system (see sensitivity section below). This prompted us to re-examine the notion that the glutathione couple acts as a redox buffer.

If the glutathione couple acts as a redox buffer, then its redox potential should have a low sensitivity to changes in the balance between reduced and oxidized glutathione species[37]. We therefore determined whether the redox potentials we measured are located in a region of the Nernst curve where glutathione could be expected to act as a buffer of redox potential. Because the oxidation of GSH into GSSG is a bimolecular reaction, E_{GSH} depends not only on the oxidation state of the glutathione couple (OxD_{GSH}), *i.e.* the amount of glutathione in its oxidized form (2[GSSG]) relative to total glutathione (GSH_{tot} = [GSH] + 2[GSSG]), but also explicitly on total glutathione GSH_{tot}. To determine OxD_{GSH} we assumed physiologically plausible values for GSH_{tot} in the range of 1–20 mM, with 10 mM being at the high end of physiological estimates[38]. We placed the E_{GSH} values we measured in the cytosol of cells in the pharynx, intestine and PLM neurons (Fig. 2b, 3b) in the context of Nernst curves for different values of GSH_{tot}. All of these redox potentials fall in a highly sensitive, non-buffering region of the Nernst curve, where even slight changes in OxD_{GSH} lead to large changes in E_{GSH} (Fig. 5a). For example, in a cell that exhibits the average cytosolic E_{GSH} of pm3 muscles (–270 mV), the value of OxD_{GSH} would be 0.0019 assuming a GSH_{tot} of 10 mM. The sensitivity of E_{GSH} to changes in OxD_{GSH} (the slope of the Nernst curve) around this OxD_{GSH} value is 88 times higher than it would be if the glutathione couple were best positioned to buffer redox potential (Fig. 5b). This relative sensitivity rises to 696 fold if we assume that GSH_{tot} is 1 mM, at the low end of physiological estimates. We conclude that the glutathione couple does not act as a buffer of redox potential, as previously thought. This result holds for GSH_{tot} values up to 1 M.

As an independent confirmation of this finding, we evaluated recent measurements of glutathione oxidation in *C. elegans* derived from studies that did not involve genetically-encoded sensors. These biochemical measurements on whole-worm extracts directly yield OxD_{GSH} values of 0.028 (ref. [39]) to 0.035 (ref. [40]). These extracts average OxD_{GSH} over all cellular compartments, including the highly-oxidizing endoplasmic reticulum, where OxD_{GSH} equals 0.4 (ref. [41]). It is not surprising, therefore, that these reported values are higher by an order of magnitude than the *in vivo* values we obtained with our targeted cytosolic sensor. Still, even if cytosolic OxD_{GSH} were equal to the values derived from whole-worm extracts, glutathione redox potential would not be buffered (Fig. 5).

Glutathione oxidation varies between individuals

What are the mechanisms that cause isogenic animals to have different sensor's redox potentials? The observed differences in redox potential between individuals could be explained by individual differences in the fraction of oxidized glutathione. However, they could also be due to individual differences in total glutathione content. The properties of the Nernst curve allow us to determine which of these two scenarios is dominant, because changes in glutathione oxidation state affect sensitivity (the slope of the Nernst curve, Fig. 5b), whereas changes in total glutathione do not affect sensitivity at any glutathione oxidation state (they only shift the Nernst curve vertically, Fig. 5a). To distinguish between these possibilities, we determined if the magnitude of the animal's redox response upon shift

to a more oxidative environment is predicted by the redox potential of the glutathione couple prior to such shift. If differences in total glutathione were the main source of redox potential variation across individuals, the sensitivities associated with different redox potentials would exhibit little or no variation and, therefore, we would not observe a correlation between redox potential and redox displacements upon oxidative shift. On the other hand, if the variation in redox potential across individuals stemmed from differences in the fraction of oxidized glutathione, we would observe a negative correlation between redox potential and the change in redox potential upon oxidative shift. Absent this Nernst framework, the latter case appears counterintuitive, since it states that animals with higher levels of protein oxidation prior to oxidant exposure would be less sensitive to oxidant treatment than animals with lower initial oxidation levels.

We recorded time-series of the sensor's redox potential in the pharynx of 64 individuals before and after shifting them to media containing 5 mM tert-butyl hydroperoxide (*t*-BuOOH). This oxidant does not react with protein thiols directly[42]; rather, it is thought to act by oxidizing GSH into GSSG, which, in turn, leads to the formation of a disulfide bond within roGFP1_R12. A representative spatio-temporal series shows that different regions along the A-P axis of the pharynx exhibit distinct responses (Fig. 6a). We quantified the time-dependent change in the sensor's redox potential of pm3, pm5 and pm7 muscles relative to their baseline redox potential (defined as the average redox potential prior to oxidant exposure; Fig. 6b–d and Supplementary Fig. 10). Each of these muscles exhibits a distinct response (Fig. 6e). While all muscles experience an increase in the sensor's redox potential after oxidant exposure, only pm5 and pm7 exhibit an adaptive response consisting of a rise and subsequent decrease in redox potential. In addition to these regularities in the response behavior of each muscle, we observed a substantial variation across individuals in the magnitude of the response to oxidant treatment (Fig. 6b–d and Supplementary Fig. 10,11). Animals with a higher baseline (colored in red, Fig. 6b–d, Supplementary Fig. 10) exhibit smaller redox displacements than animals with a lower baseline (colored in blue). This relation is confirmed by the negative sign of the observed strong correlations between baselines and early redox displacements of pm3, pm5 and pm7 muscles (Fig. 6f). Thus, the response dynamics that we observe indicate that differences in baseline across individuals are due in large part to differences in glutathione oxidation, not glutathione content.

Sensitivity of protein oxidation to E_{GSH} variation

In our study we encountered differences in the sensor's redox potential across individuals (13 mV), across tissues (2.8 mV), within tissues (7.5 mV), across genetic perturbations (4.2 mV) and under oxidative stress (15 mV). To understand how much these differences may impact protein oxidation, we considered the effect of E_{GSH} variation on the thiol-disulfide balance on protein targets in equilibrium with the glutathione couple.

Changes in the glutathione redox potential sway the oxidation states of target proteins in the same direction, but the magnitude depends on both the protein's tendency to remain reduced (quantified by its midpoint potential) and its initial oxidation state (determined by the redox potential it was experiencing). Midpoint potentials are presently unknown for most proteins. Still, we can treat them as variables and analyze the impact of a redox-potential change on

protein oxidation, both in terms of absolute differences and fold changes (Fig. 7). For example, a difference in glutathione redox potential of 10 mV that we typically observe in response to 5 mM *t*-BuOOH treatment would affect the oxidized fraction of a protein by at most 19% (absolute difference; Fig. 7b) or by a factor of at most 2.2 (fold change; Fig. 7c). Such changes can be biologically significant, especially given the wide variety of redox-sensitive proteins.

DISCUSSION

The study of the regulation of cytosolic glutathione redox potential has been challenging, especially in live multicellular organisms. The methods used until recently required the homogenization of samples, resulting in the mixing of sub-cellular compartments, cells, tissues, and often entire populations. In this study, we overcame this difficulty by using a genetically-encoded protein sensor. The ability to visualize and quantify the sensor's redox potential in live individuals, at cellular and high temporal resolution, made it possible to investigate the structure and regulation of the cytosolic glutathione redox potential, as well as the determinants of its variation. As we discuss below, this variation reflects, in part, the high sensitivity of this potential to changes in glutathione oxidation. The regulation of the sensor's redox potential is suggested by (i) differences in the average redox potentials of pharynx, intestine and PLM neurons; (ii) the spatial patterning of the sensor's redox potential along the anterior-posterior axis of the pharynx; and (iii) differences in the response dynamics to oxidant treatment of individual pharyngeal muscles.

We found that the action of insulin signaling affects the spatial organization of the sensor's redox potential. The insulin receptor DAF-2 regulates this redox potential in the cytosol in a tissue-specific manner, affecting it in pharyngeal muscles and intestine, but not in PLM neurons. In addition, DAF-2 contributes quantitatively to the spatial patterning of redox potential in the pharynx by regulating the activity of the FOXO transcription factor DAF-16. We also found that a *daf-2* mutation that causes type-A insulin resistance in humans is sufficient to lower the cytosolic redox potential of the glutathione couple, which may lead to a significant decrease in the oxidation of target proteins. It would be interesting to investigate whether similar changes in the thiol-disulfide balance are important to the pathogenesis of insulin resistance and diabetes in humans.

Glutathione has been widely thought to act as the main redox buffer of the cell[1, 35, 36], a function that provides homeostasis by protecting proteins from the indirect oxidizing action of reactive oxygen species. This view seemed difficult to reconcile with the considerable variation in glutathione redox potential across isogenic individuals, since this variation might cause significant differences in protein oxidation levels. In an effort to substantiate whether the glutathione couple acts as a redox buffer in the cytosol, we found that it does the opposite.

The notion of glutathione as a redox buffer may have gained traction over the last half century because the abundant glutathione restores protein thiols that underwent oxidative attack and reduces oxidants such as hydrogen peroxide. Yet, this very action produces an oxidant, glutathione disulfide (GSSG). Because most cytosolic glutathione is reduced *in*

vivo, an ever so slight change in GSSG concentration strongly affects the glutathione redox potential (Fig. 5)[43]. Changes in the glutathione redox potential will have repercussions on a much wider array of cysteine thiols than those that were initially threatened by oxidative attack, because cysteine thiols generally react *in vivo* very slowly with hydrogen peroxide but much faster with GSSG[42, 44].

Our results call for a change in perspective on the role of the cytosolic glutathione couple. Numerous redox couples, including H_2O_2/H_2O and $NADP^+$/NADPH, interact with the glutathione couple. As a result, the relative levels of GSH and GSSG are determined by a wide range of concurrent processes, including those that generate hydrogen peroxide and those that influence the production or utilization of $NADP^+$ and NADPH. Because the glutathione couple is not positioned to buffer its redox potential in the cytosol, this potential responds sensitively to changes in glutathione oxidation. We therefore propose that the glutathione couple integrates and amplifies the effects of diverse redox inputs into a single physiological signal: the glutathione redox potential (Fig. 8), to which proteins with embedded cysteines can respond differentially.

The glutathione couple can be thought of as a broker that mediates the indirect effects of oxidants and reductants on the thiol-disulfide balance of many proteins. Because the activity of proteins can be affected by this balance, the high sensitivity of E_{GSH} to changes in glutathione oxidation may enable cells to respond to very small changes in the concentration of these reactive chemical species, well before their concentration is high enough to be toxic. This form of intracellular signaling may enable cells to mount an adaptive response to counteract the toxicity of a subsequent and more massive exposure to one of these reactive species. Indeed, disulfide bond formation in direct regulators of Nrf2 and NFκB increases transcription by these factors, which plays an important role in the cellular response to oxidants[7, 45].

What would happen if the glutathione couple acted as a redox buffer? We expect that thioldisulfide modification of in principle responsive proteins would become insensitive to redox events that affect the fraction of oxidized glutathione, since those events would no longer entail significant changes in redox potential. For example, the same change in glutathione oxidation that results in a 10 mV increase in E_{GSH} when the couple is in a highly-sensitive region of the Nernst curve (OxD_{GSH} = 0.0019, GSH_{tot} = 10 mM), would only cause a 0.165 mV increase if the couple were optimally positioned as a buffer. As can be seen in Fig. 7, under buffering conditions, such an event would no longer lead to a change in the thiol-disulfide balance of the protein network targeted by glutathione.

Because the glutathione couple is so abundant[1], the concentration of GSSG in the cytosol remains significant compared to the typical concentrations of cytosolic proteins, even though most glutathione is in the reduced form. We estimate that GSSG concentration is about 9 μM in the average pm3 muscle of *C. elegans* (OxD_{GSH} = 0.0019, assuming GSH_{tot} = 10 mM). This concentration is comparable to the 1 μM median concentration of cytosolic proteins in yeast[46, 47] and is only slightly lower than the concentration of abundant cytosolic proteins (*e.g.* the concentrations of ten glycolytic enzymes in mammalian muscle ranges between 29–131 μM[48]). A 9 μM GSSG concentration is also much higher than the 0.001–

0.7 μM physiological concentration range of cytosolic hydrogen peroxide in aerobic organisms[49]. Therefore, the kinetics of thiol-disulfide exchange between the glutathione couple and its target protein couples are not likely to be limited by the concentrations of GSSG and GSH. This means that the glutathione couple is well positioned to mediate efficiently the transfer of electrons to and from its target proteins.

The differences in glutathione redox potential that we observe in the *C. elegans* pharynx reflect the population's diversity, rather than the individual's variation over time, since individuals have essentially stable glutathione redox potentials over the course of almost an hour (Supplementary Fig. 2). It is notable that individuals can exhibit distinct and stable glutathione redox potentials, since those differences must arise as a result of miniscule differences in glutathione oxidation. For example, the entire 12 mV range of pharyngeal E_{GSH} values would be due to OxD_{GSH} values between 0.0012 and 0.0028, assuming GSH_{tot} = 10 mM for all animals. This means that *C. elegans* is able to control glutathione oxidation with great precision. Thus, the thiol-disulfide balance of the network of proteins targets of the glutathione couple is capable of both stability (as a result of the control of glutathione oxidation) and sensitivity (as a result of the high-sensitivity of glutathione redox potential to changes in glutathione oxidation).

The vast majority of cytosolic glutathione (>99%) is found in the reduced state in a wide range of cell types and organisms[1]. For example, cytosolic OxD_{GSH} is 0.00004 in yeast[43], 0.0007 in cultured human HeLa cells[21, 50], 0.0066 in rat liver[1] and 0.009 in *E. coli*[51]. When placed in the context of the Nernst curve, these OxD_{GSH} values indicate that the glutathione couple is positioned in the highly sensitive, non-buffering region of the curve in all of these organisms (Fig. 5). Thus, this property is not unique to *C. elegans*.

In the *C. elegans* pharynx, variation in OxD_{GSH} values between individuals leads to differences in the magnitude of their response to tert-butyl hydroperoxide treatment. Similarly, variation in OxD_{GSH} values across species suggests large differences in redox sensitivity to changes in glutathione oxidation. For example, we predict yeast to be 159-fold more sensitive than rat liver cells to a small change in OxD_{GSH}. It would be interesting to explore what adaptive constrains caused species to position their glutathione couple to provide different redox sensitivities.

While the glutathione couple facilitates a sensitive regulation of the thiol-disulfide balance of target proteins in the cytosol, it may well play a buffering role in other sub-cellular compartments. Redox potential is optimally buffered by the glutathione couple when OxD_{GSH} equals 0.414 (Fig. 5b). This optimal value is in excellent agreement with measured OxD_{GSH} values of 0.4 in the endoplasmic reticulum[41, 50]. We conclude that, unlike in the cytosol, the glutathione couple is positioned to buffer the thiol-disulfide balance of target proteins in the endoplasmic reticulum.

The glutathione couple's capacity to sensitively affect the thiol-disulfide balance of its target protein network may be advantageous by enabling organisms to respond to small perturbations to the cytosolic redox environment. However, this sensitivity could also amplify the effects of any breakdown in cellular redox homeostasis, setting the stage for the

association between cytosolic redox changes and the etiology and progression of many human diseases, particularly those for which aging is a strong risk factor[9, 10, 11].

METHODS

Strains and culture

C. elegans were cultured under standard conditions at 20°C. Wild-type *C. elegans* was Bristol N2.

Construction of transgenes

We built roGFP1_R12 from the vector pPD96_32 (Fire vector kit, Addgene), which contains a GFP construct optimized for expression efficiency in *C. elegans*. We replaced seven residues in this construct (C48S, C65S, S147C, N149K, S202K, Q204C, F223R) by site-directed mutagenesis (QuickChange, Stratagene) to generate roGFP1_R12 (ref. [23]). We used a combination of classical cloning and fusion-PCR to remove the mitochondrial-targeting sequence in the original plasmid and to fuse the roGFP1_R12 coding sequence to specific promoters. The fusion-PCR for the coding region was done with 12-cycles of amplification to minimize the chances of introducing sequence errors (Expand High Fidelity PCR System, Roche), and cloned into a TOPO BluntII vector. We confirmed the sequence for all the constructs injected by DNA sequencing, using the primers listed in Supplementary Table 4.

roGFP1_R12 expression in pharyngeal muscle—We amplified the *myo-2* promoter from pPD80.08 (Fire vector kit, Addgene) with primers WF45 and WF46, and cloned the PCR product into a TOPO BluntII vector. *roGFP1_R12* was inserted into this vector backbone by restriction with AgeI and BswiWI, generating *Pmyo-2*: :*roGFP1_R12*.

roGFP1_R12 expression in intestine—We amplified the *sur-5* promoter from pPD158.87 (Fire vector kit, Addgene) with primers WF45 and WF49, and cloned the PCR product into a TOPO BluntII vector. We fused this promoter to a restriction fragment containing *roGFP1_R12* by secondary PCR using primers WF38 and WF129, generating *sur-5*: :*roGFP1_R12*. Although we expected the *sur-5* promoter to drive roGFP1_R12 expression in several tissues, we found that our transgenic lines exhibit high expression of roGFP1_R12 only in the intestine at the 100X magnification we used for imaging animals throughout this study.

roGFP1_R12 expression in motorneurons—We amplified the *mec-4* promoter from *C. elegans* genomic DNA with primers WF96 and WF99, and cloned the PCR product into a TOPO BluntII vector. *roGFP1_R12* was inserted into this vector backbone by restriction with AgeI and PstI, generating *Pmec-4*: : *roGFP1_R12*.

Generation of transgenic animals and construction of strains

The plasmids containing *Pmyo-2*: :*roGFP1_R12* and *Pmec-4*: :*roGFP1_R12* were microinjected using *rol-6(su1006)* as coinjection marker. The plasmid containing *Psur-5*: :*roGFP1_R12* was microinjected without a coinjection marker.

Pmyo-2: :*roGFP1_R12*, *Pmec-4*: :*roGFP1_R12* and *Psur-5*: :*roGFP1_R12* were microinjected into wild-type at concentrations ranging from 15 to 50 ng/μl, to generate *ydEx20* and *ydEx40*; *ydEx37* and *ydEx42*; and *ydEx25*, *ydEx22* and *ydEx24* respectively. *ydEx20* was integrated into the genome by irradiation with ultraviolet light (254 nm), generating *ydIs1*. After integration the strain was outcrossed six times to wild type. Double and triple mutants were generated by standard genetic methods. Unless noted, measurements in pharynx, PLM neurons and intestine were performed in *ydIs1*, *ydEx37* and *ydEx25* animals, respectively. gcs-1(ok436)/unc-4(e120) oxIs322[Cb-unc-119(+), Pmyo-2: :mCherry: :H2B, Pmyo-3: :mCherry: :H2B]; *ydEx20*, was derived by crossing *gcs-1(ok436)/mIn1[mIs14 dpy-10(e128)]* males with *unc-4(e120) oxIs322; ydEx20* hermaphrodites. The 25°C Daf-c phenotype was used to identify *daf-2(e1370)* and *daf-2(m579)* mutants. *daf-16(mu86)* and *daf-16(+)* were distinguished by PCR[33]. Transgenes were identified based on the presence of green fluorescence in pharynx (*ydIs1*, *ydEx20* and *ydEx40*), mechanosensory neurons (*ydEx37* and *ydEx42*) and intestine (*ydEx25*, *ydEx22 and ydEx24*). *oxIs322* was identified based on the presence of red fluorescence in the pharynx.

Live microscopy

We performed live fluorescence measurements in petri dishes (50 × 9 mm, Falcon). We modified the standard NGM (Nematode Growth Media) to optimize imaging conditions. The modified media (which we refer as “NIM”, for Nematode Imaging Media) does not contain peptone and contains agarose instead of agar (to minimize the fluorescence of the media upon illumination with 410 and 470 nm light); it also does not contain $CaCl_2$ (to prevent the formation of a precipitate that reduces light transmittance), nor cholesterol and $MgSO_4$ (normally included to support long-term nematode culture, but dispensable in the short time scales of imaging). The use of NIM resulted in 3.5 and 2.6 fold background reductions in the 410 and 470 nm channels, respectively. This optimized media produced background levels equal to only 1.6 and 1.4 times the camera noise in those channels. To prepare 100 mL of NIM, 2 g agarose and 0.3 g NaCl were dissolved in 96.5 mL of water and melted in a microwave. When the solution cooled down to 50°C we added 2.5 mL 1 M K_2HPO_4/KH_2PO_4 pH 6.0 and 1 mL 1 M levamisole. We poured 7 mL of NIM per petri dish, air dried the plates at room temperature for 1 hour, stored them at 4°C, and used them within two weeks. Animals were staged by transferring 30 to 50 late L4 hermaphrodite larvae to NGM plates (Fig. 1,2,4a–c, Supplemental Fig.1); or NGM plates with 4.5 μg/ml FUDR (Fig. 3, 4d–e, 6), with each plate being considered as a technical replicate. For all experiments at least two replicates per condition were considered during the same day of imaging, and measurements were performed in two different days at least, providing a minimum of four technical replicates. Imaging was conducted between 44 and 52 hours after transfer (day 2 of adulthood), except for Fig. 1 and Supplementary Fig. 1 (day 1 of adulthood) and Supplementary Fig. 2 (L2 larval stage). Before imaging, worms were transferred to NIM plates at room temperature (21–23°C) for 90 min. The imaging order between conditions was randomized.

Imaging hardware and illumination

Imaging was conducted on a motorized Axioskop 2 FS plus microscope (Zeiss) using a Plan-Apochromat 10X 0.45 NA 2 mm working distance objective lens (1063–139, Zeiss). Imaging plates were controlled by a motorized stage (ProScan II, Prior) with a stage-mounted customized Petri dish holder. Images were acquired with Metamorph 7.5.3.0 software. All microscopy was performed at 22°C. Excitation at 410 nm and 470 nm was performed sequentially with a high-speed filter changer (Lambda DG-4, Shutter Instrument Company) controlling the excitation filters D410/30x and D470/20x. The filtered light was reflected by a 500dcxr dichroic mirror to illuminate the specimen. The emitted fluorescence passed through the filter HQ535/50m and was detected with a Cool SNAP HQ^2 14-bit camera (Photometrics). All filters were manufactured by Chroma.

Optimization of microscopy for different tissues

We optimized exposure times to use at least two thirds of the dynamic range of the camera. This step ensures that image segmentation is performed consistently across all experimental conditions and for all imaged tissues, making of the automatic image segmentation a blinded process for the researcher. We choose the camera binning based on the spatial resolution required for tissues of different morphology and size. To image the feeding muscles of the pharynx, we focused on the plane of the pharyngeal lumen under transmitted light. Fluorescence images were acquired with 4×4 binning using an average exposure time of 40 ms (Fig. 1,2,4,6). Higher spatial resolution images were acquired with 2×2 binning, with average exposure times of 165 ms and 300 ms, respectively for Fig. 3 and Supplementary Fig. 3. In control experiments we imaged 20 animals sequentially with 2×2 and 4×4 binning and found that the resulting estimates of the ratio of fluorescence ($R_{410/470}$) are highly correlated ($r = 0.961$, $p < 0.0001$). To image the intestine, we concentrated on the posterior region of the tissue, which exhibits higher sensor expression. Fluorescence images were acquired with 4×4 binning, using average exposure times of 105 ms. To image mechanosensory neurons, we selected the PLMs neurons because they are located at the tail of the worm were the specimen is thin and flat and, therefore, short focal depth is required for imaging. Only one of the two PLM neurons was quantified for each worm. Fluorescence images were acquired with 2×2 binning using average exposure times of 450 ms.

Image processing and segmentation

Image processing was conducted in ImageJ (NIH) and Matlab (Mathworks). We performed background subtraction by removing the mode intensity value of the entire image from each pixel. This procedure removes the background due to the agar and the camera noise, since the vast majority of pixels in our images were part of the background. To segment the images, we defined regions of interest (ROI) by applying a threshold in the 410 nm excitation images. We used the same intensity value for the segmentation across all tissues and conditions. In the case of PLM neurons the ROIs correspond to single cells; in the case of intestine the ROIs correspond to the most posterior portion of the tissue (approximately 85 μm in length); in the case of feeding muscles the ROIs correspond to the entire pharynx. We use the ROIs to quantify both the 410 nm and 470 nm excitation images (I_{410} and I_{470}

images, respectively). We obtained nearly identical $R_{410/470}$ values by segmenting based on I_{410} or I_{470} images ($r = 0.999$, $p < 0.0001$, for the individuals in Fig. 3).

Ratiometric measurements

We calculated $R_{410/470}$ by computing the ratio of the total fluorescence between the segmented I_{410} and I_{470} regions. To study how $R_{410/470}$ and its transforms vary along the anterior-posterior (A-P) axis of the pharynx, we generated $R_{410/470}$ profiles along the midline of this tissue using automated scripts in ImageJ. First, the segmented I_{410} and I_{470} regions were rotated, centered and reflected to orient them along their A-P axis. We then constructed a polyline in the I_{410} image along the midline of the pharynx using features of five morphological pharyngeal landmarks. This polyline was visually inspected and, when necessary, adjusted manually to ensure the quality of the alignment to the midline of each pharynx. We refer to this polyline as the "medial axis of the pharynx", and measurements conducted along the medial axis as "anterior-posterior pharyngeal profiles". We measured the intensity along the medial axis in I_{410} and I_{470} images, using a line width of 5.16 μm (2 pixels) for 4×4 binning images and a line width of 7.74 μm (6 pixels) for 2×2 binning images. The resulting intensity vectors were then length-normalized using bilinear interpolation. We determined the E profile along the A-P axis of the pharynx from the computed element-wise intensity ratios (I_{410}/I_{470}) between these two vectors. We note that the average value of E for the medial axis (the ratio of 410 to 470 total fluorescence along the medial axis) approximates very closely that of the whole pharynx ($r = 0.9988$, $p < 0.0001$ for the 394 animals in Fig. 3). To calculate the value of E for individual muscle segments, we identified muscle boundaries based on the position of the morphological landmarks of the pharynx in the length-normalized intensity vectors. We computed E from the ratio of the 410 and 470 nm total intensities within each region.

Image visualization

Pixel-by-pixel E images, computed from the raw unsegmented I_{410} and I_{470} images, provide a valuable visualization tool that complements the formal image analysis and quantification described above. We computed E from pixel-by-pixel $R_{410/470}$ values, and generated RGB images by mapping E values to a colormap. We wanted these images to provide information about the magnitude of the intensity signals utilized; de-emphasizing pixels where the signal was low. To this end, we adjusted the brightness of pixels whose intensity values in the I_{410} or I_{470} images were below the value of the intensity cutoff used for segmentation (equal to 2000 in all images shown). Images were transformed to the hue-saturation-brightness (HSB) color space, and pixels with intensity values above the cutoff were assigned a brightness value of 1, while those with intensities below the cutoff were assigned a brightness value equal to their intensity divided by the cutoff value. The resulting HSB image was transformed to RGB for visualization. We used the cool-warm and similar diverging colormaps[52] to color-code images and pharyngeal E profiles, as these colormaps are perceptually linear and behave well for observers with color-deficient vision.

Determination of OxD_{roGFP} and E_{roGFP} from $R_{410/470}$

In order to calculate the fraction of roGFP1_R12 molecules with a disulfide bond (OxD_{roGFP}) from ratiometric fluorescence measurements[17], we determined empirically the value of the three parameters relating OxD_{roGFP} to $R_{410/470}$, as described in the legend of Fig. 1. We note that the parameter α determines the curvature of the relationship from $R_{410/470}$ to OxD_{roGFP} (if α were equal to 1, then the relationship in Fig.1e would be linear). We treated worms with various concentrations of oxidants and reductants and found that the sequential treatment with the oxidant diamide (50 mM, Sigma) followed by treatment with the reducing agent dithiothreitol (DTT, 100 mM, Sigma), resulted in maximal oxidation and reduction of the sensor, respectively, in the pm3 muscles of the pharynx. The *in vivo* dynamic range of the sensor matched the reported *in vitro* dynamic range[23]. These experiments also showed that 50 mM diamide treatment and 100 mM DTT treatment affect the expression of the roGFP1_R12 sensor and GFP S65C by at most 10%, in the timescale of the Fig. 1 experiment. All chemical incubations were performed in NIM plates. No photobleaching was observed during incubations.

We calculated the potential of the redox couple defined by oxidized and reduced forms of roGFP1_R12 using the Nernst equation $E = E^{\circ\prime} - [RT/(2F)] \ln [(1-OxD_{roGFP})/OxD_{roGFP}]$, with the standard roGFP1_R12 half-cell reduction potential ($E^{\circ\prime}$) of −265 mV (ref [23]), a temperature of 295.15 (22°C), and assuming a cytosolic pH of 7. The final relation from $R_{410/470}$ to E_{roGFP} is given by the expression $E_{roGFP} = E^{\circ\prime}{}_{roGFP} - [RT/(2F)] \ln \{[\alpha (R_{ox} - R_{410/470})] / (R_{410/470} - R_{red})\}$. It is noteworthy that the parameter α shifts E_{roGFP} by a constant value equal to $- [RT/(2F)] \ln \alpha$. As a result, E_{roGFP} differences are not affected by this parameter. We also note that while the value of E_{roGFP} is influenced by pH (by shifting the midpoint potential of the couple), under physiological conditions these effects are not relevant to understand the equilibration of potentials between roGFP1_R12 and GSH couples[1, 17]. This is because, both couples involve the exchange of two protons and two electrons and, under physiological conditions, pH is well below the pK_a of the reactant thiols (pK_a = 8.92 for GSH and ~9.0 for roGFP1_R12 C147 and C204); as a result, the midpoint potentials of these redox couples are affected by pH in the same direction and by essentially the same amount[17, 23, 53]. We also note that the fluorescence ratio emitted by roGFP1 is unaffected by changes in pH in the physiological range (6.0–8.5)[19], which encompass the reported 6.9–7.5 range in cytosolic pH of *C. elegans* intestine and 7.5 cytosolic pH of *C. elegans* body muscle[54, 55].

Ratiometric measurements in *gcs-1* mutants

The *gcs-1(ok436)/unc-4(e120) oxIs322*; *ydEx20* strain was used as a parental strain in experiments with the *gcs-1* mutant. *gcs-1(ok436)* homozygous progeny from that strain were identified by the lack of mCherry pharyngeal expression. These *gcs-1(maternal+zygotic−)* animals arrested during larval development. Their *gcs-1(maternal+zygotic+)* siblings expressed mCherry in the pharynx and did not arrest larval development. Ratiometric measurements were performed in pm3 muscles at the L2 larval stage.

tert-butyl hydroperoxide assays

We treated animals with 5 mM *tert*-butyl hydroperoxide (*t*-BuOOH), in freshly made imaging plates (used within 4 hours of preparation). $R_{410/470}$ time series in untreated individual worms were acquired for 10 min prior to *t*-BuOOH treatment. Individual worms were then transferred to plates with 5 mM *t*-BuOOH and imaged for additional 60 min, with a gap of 3 to 6 minutes between treatments. Images were acquired every 30 seconds.

Statistical analysis

All statistical analyses were performed in JMP (SAS) and Matlab (Mathworks). We tested for differences in the average *E* among groups using ANOVA. We used the Tukey HSD post-hoc test to determine which pairs of groups in the sample differ, in cases where more than two groups were compared. We used least-squares regression to quantify genetic interactions between wild-type and mutant alleles of *daf-2* and *daf-16* using the following linear model: $E = \text{Intercept} + daf\text{-}2 + daf\text{-}16 + daf\text{-}2 * daf\text{-}16 + \varepsilon$. The second to last term in this model quantifies the existence, magnitude and type (synergistic or antagonistic) of genetic interaction between *daf-2* and *daf-16* mutant alleles.

Functional data analysis (FDA)

We used the FDA statistical package in Matlab[56] to model and analyze positional-series of *E* values in pharyngeal A-P profiles and time-series of *E* values in the response to *t*-BuOOH. The basic idea of this approach is to express discrete spatial or temporal series of observations in the form of a function. These functions are then treated as single observations, which are analyzed statistically applying concepts of multivariate analysis[34]. A more detailed description of our application of this technique is given in the Supplementary Methods.

Supplementary Material

Refer to Web version on PubMed Central for supplementary material.

Acknowledgments

We thank Timothy Mitchison, Jennifer Whangbo, Rebecca Ward, Eric Deeds, Daniel Yamins and Nina Fedoroff for critical reading and detailed comments on our manuscript. Bernd Moosmann kindly provided the number of cysteines in the *C. elegans* proteome. We benefitted from discussions with Nicholas Stroustrup, Thomas Kolokotrones and Tami Lieberman. Some strains were contributed by the CGC, which is funded by the NIH Office of Research Infrastructure Programs (P40 OD010440). The research was in part supported by a project grant from the Paul F. Glenn Laboratories for the Biological Mechanisms of Aging at Harvard Medical School and the National Institute of Health through grant R01 AG034994.

REFERENCES

1. Gilbert HF. Molecular and cellular aspects of thiol-disulfide exchange. Adv Enzymol Relat Areas Mol Biol. 1990; 63:69–172. [PubMed: 2407068]
2. Gilbert HF. Biological disulfides: the third messenger? Modulation of phosphofructokinase activity by thiol/disulfide exchange. J Biol Chem. 1982; 257:12086–12091. [PubMed: 6214556]
3. Corcoran A, Cotter TG. Redox regulation of protein kinases. FEBS J. 2013; 280:1944–1965. [PubMed: 23461806]

4. Fuller W, Tulloch LB, Shattock MJ, Calaghan SC, Howie J, Wypijewski KJ. Regulation of the cardiac sodium pump. Cell Mol Life Sci. 2013; 70:1357–1380. [PubMed: 22955490]
5. Yang Y, Jin X, Jiang C. S-glutathionylation of ion channels: insights into the regulation of channel functions, thiol modification crosstalk and mechanosensing. Antioxid Redox Signal. 2013
6. de Keizer PL, Burgering BM, Dansen TB. Forkhead box o as a sensor, mediator, and regulator of redox signaling. Antioxid Redox Signal. 2011; 14:1093–1106. [PubMed: 20626320]
7. Pastore A, Piemonte F. S-Glutathionylation signaling in cell biology: progress and prospects. Eur J Pharm Sci. 2012; 46:279–292. [PubMed: 22484331]
8. Sakai J, et al. Reactive oxygen species-induced actin glutathionylation controls actin dynamics in neutrophils. Immunity. 2012; 37:1037–1049. [PubMed: 23159440]
9. Xiong Y, Uys JD, Tew KD, Townsend DM. S-glutathionylation: from molecular mechanisms to health outcomes. Antioxid Redox Signal. 2011; 15:233–270. [PubMed: 21235352]
10. Sabens Liedhegner EA, Gao XH, Mieyal JJ. Mechanisms of altered redox regulation in neurodegenerative diseases--focus on S--glutathionylation. Antioxid Redox Signal. 2012; 16:543–566. [PubMed: 22066468]
11. Mieyal JJ, Gallogly MM, Qanungo S, Sabens EA, Shelton MD. Molecular mechanisms and clinical implications of reversible protein S-glutathionylation. Antioxid Redox Signal. 2008; 10:1941–1988. [PubMed: 18774901]
12. Sanchez-Gomez FJ, Espinosa-Diez C, Dubey M, Dikshit M, Lamas S. S-glutathionylation: relevance in diabetes and potential role as a biomarker. Biol Chem. 2013; 394:1263–1280. [PubMed: 24002664]
13. Holmgren A. Thioredoxin and glutaredoxin systems. J Biol Chem. 1989; 264:13963–13966. [PubMed: 2668278]
14. Meyer Y, Buchanan BB, Vignols F, Reichheld JP. Thioredoxins and glutaredoxins: unifying elements in redox biology. Annu Rev Genet. 2009; 43:335–367. [PubMed: 19691428]
15. Jones DP. Radical-free biology of oxidative stress. Am J Physiol Cell Physiol. 2008; 295:C849–868. [PubMed: 18684987]
16. Moosmann B, Behl C. Mitochondrially encoded cysteine predicts animal lifespan. Aging Cell. 2008; 7:32–46. [PubMed: 18028257]
17. Meyer AJ, Dick TP. Fluorescent protein-based redox probes. Antioxid Redox Signal. 2010; 13:621–650. [PubMed: 20088706]
18. Meyer AJ, et al. Redox-sensitive GFP in Arabidopsis thaliana is a quantitative biosensor for the redox potential of the cellular glutathione redox buffer. The Plant journal : for cell and molecular biology. 2007; 52:973–986. [PubMed: 17892447]
19. Schwarzlander M, et al. Confocal imaging of glutathione redox potential in living plant cells. J Microsc. 2008; 231:299–316. [PubMed: 18778428]
20. Ostergaard H, Tachibana C, Winther JR. Monitoring disulfide bond formation in the eukaryotic cytosol. J Cell Biol. 2004; 166:337–345. [PubMed: 15277542]
21. Gutscher M, et al. Real-time imaging of the intracellular glutathione redox potential. Nat Methods. 2008; 5:553–559. [PubMed: 18469822]
22. Albrecht SC, Barata AG, Grosshans J, Teleman AA, Dick TP. In vivo mapping of hydrogen peroxide and oxidized glutathione reveals chemical and regional specificity of redox homeostasis. Cell Metab. 2011; 14:819–829. [PubMed: 22100409]
23. Cannon MB, Remington SJ. Re-engineering redox-sensitive green fluorescent protein for improved response rate. Protein Sci. 2006; 15:45–57. [PubMed: 16322566]
24. Hanson GT, et al. Investigating mitochondrial redox potential with redox-sensitive green fluorescent protein indicators. J Biol Chem. 2004; 279:13044–13053. [PubMed: 14722062]
25. Kosower NS, Kosower EM. Diamide: an oxidant probe for thiols. Methods Enzymol. 1995; 251:123–133. [PubMed: 7651192]
26. Liao VH, Yu CW. Caenorhabditis elegans gcs-1 confers resistance to arsenic-induced oxidative stress. Biometals. 2005; 18:519–528. [PubMed: 16333752]
27. Mango SE. The C. elegans pharynx: a model for organogenesis. WormBook. 2007:1–26. [PubMed: 18050503]

28. Honda Y, Honda S. The daf-2 gene network for longevity regulates oxidative stress resistance and Mn-superoxide dismutase gene expression in Caenorhabditis elegans. Faseb J. 1999; 13:1385–1393. [PubMed: 10428762]
29. Holzenberger M, et al. IGF-1 receptor regulates lifespan and resistance to oxidative stress in mice. Nature. 2003; 421:182–187. [PubMed: 12483226]
30. Kimura KD, Tissenbaum HA, Liu Y, Ruvkun G. daf-2, an insulin receptor-like gene that regulates longevity and diapause in Caenorhabditis elegans. Science. 1997; 277:942–946. [PubMed: 9252323]
31. Patel DS, et al. Clustering of genetically defined allele classes in the Caenorhabditis elegans DAF-2 insulin/IGF-1 receptor. Genetics. 2008; 178:931–946. [PubMed: 18245374]
32. Ogg S, et al. The Fork head transcription factor DAF-16 transduces insulin-like metabolic and longevity signals in C. elegans. Nature. 1997; 389:994–999. [PubMed: 9353126]
33. Lin K, Dorman JB, Rodan A, Kenyon C. daf-16: An HNF-3/forkhead family member that can function to double the life-span of Caenorhabditis elegans. Science. 1997; 278:1319–1322. [PubMed: 9360933]
34. Ramsay, JO.; Silverman, BW. Functional data analysis. 2nd edn. Springer; 2006.
35. Schafer FQ, Buettner GR. Redox environment of the cell as viewed through the redox state of the glutathione disulfide/glutathione couple. Free Radic Biol Med. 2001; 30:1191–1212. [PubMed: 11368918]
36. Bachi A, Dalle-Donne I, Scaloni A. Redox proteomics: chemical principles, methodological approaches and biological/biomedical promises. Chem Rev. 2013; 113:596–698. [PubMed: 23181411]
37. Clark WM. Studies on Oxidation-Reduction. I. Introduction. Public Health Reports. 1923; 38:443–445.
38. Meister A. Glutathione metabolism and its selective modification. J Biol Chem. 1988; 263:17205–17208. [PubMed: 3053703]
39. Luersen K, et al. The glutathione reductase GSR-1 determines stress tolerance and longevity in Caenorhabditis elegans. PLoS One. 2013; 8:e60731. [PubMed: 23593298]
40. Arkblad EL, et al. A Caenorhabditis elegans mutant lacking functional nicotinamide nucleotide transhydrogenase displays increased sensitivity to oxidative stress. Free Radic Biol Med. 2005; 38:1518–1525. [PubMed: 15890626]
41. Bass R, Ruddock LW, Klappa P, Freedman RB. A major fraction of endoplasmic reticulum-located glutathione is present as mixed disulfides with protein. J Biol Chem. 2004; 279:5257–5262. [PubMed: 14630926]
42. Winterbourn CC, Metodiewa D. Reactivity of biologically important thiol compounds with superoxide and hydrogen peroxide. Free Radic Biol Med. 1999; 27:322–328. [PubMed: 10468205]
43. Morgan B, Ezerina D, Amoako TN, Riemer J, Seedorf M, Dick TP. Multiple glutathione disulfide removal pathways mediate cytosolic redox homeostasis. Nat Chem Biol. 2013; 9:119–125. [PubMed: 23242256]
44. Nagy, P.; Winterbourn, CC.; James, CF. Advances in Molecular Toxicology. Elsevier; 2010. Chapter 6 - Redox Chemistry of Biological Thiols.
45. Brigelius-Flohe R, Flohe L. Basic principles and emerging concepts in the redox control of transcription factors. Antioxid Redox Signal. 2011; 15:2335–2381. [PubMed: 21194351]
46. Ghaemmaghami S, et al. Global analysis of protein expression in yeast. Nature. 2003; 425:737–741. [PubMed: 14562106]
47. Milo R, Jorgensen P, Moran U, Weber G, Springer M. BioNumbers--the database of key numbers in molecular and cell biology. Nucleic acids research. 2010; 38:D750–753. [PubMed: 19854939]
48. Maughan DW, Henkin JA, Vigoreaux JO. Concentrations of glycolytic enzymes and other cytosolic proteins in the diffusible fraction of a vertebrate muscle proteome. Molecular & cellular proteomics : MCP. 2005; 4:1541–1549. [PubMed: 15982968]
49. Stone JR, Yang S. Hydrogen peroxide: a signaling messenger. Antioxid Redox Signal. 2006; 8:243–270. [PubMed: 16677071]

50. Appenzeller-Herzog C. Glutathione- and non-glutathione-based oxidant control in the endoplasmic reticulum. J Cell Sci. 2011; 124:847–855. [PubMed: 21378306]
51. Aslund F, Zheng M, Beckwith J, Storz G. Regulation of the OxyR transcription factor by hydrogen peroxide and the cellular thiol-disulfide status. Proc Natl Acad Sci U S A. 1999; 96:6161–6165. [PubMed: 10339558]
52. Moreland, K. Diverging Color Maps for Scientific Visualization. Proceedings of the 5th International Symposium on Visual Computing; 2009.
53. Wadman P. Reduction potentials of one-electron couples involving free radicals in aqueous solution. Journal of Physical and Chemical Reference Data. 1989; 18:1637–1755.
54. Pfeiffer J, Johnson D, Nehrke K. Oscillatory transepithelial H(+) flux regulates a rhythmic behavior in C. elegans. Curr Biol. 2008; 18:297–302. [PubMed: 18291648]
55. Johnson D, Allman E, Nehrke K. Regulation of acid-base transporters by reactive oxygen species following mitochondrial fragmentation. Am J Physiol Cell Physiol. 2012; 302:C1045–1054. [PubMed: 22237403]
56. Ramsay, JO.; Hooker, G.; Graves, S. Functional data analysis with R and MATLAB. Springer; 2009.

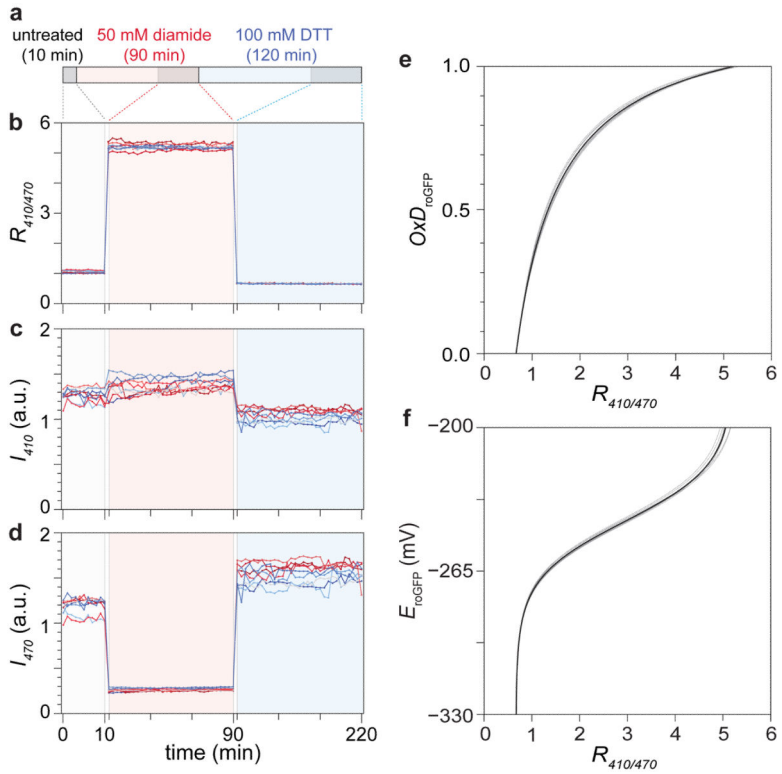

Figure 1. Measurement of roGFP1_R12 redox potential in live *C. elegans*

(**a**) Treatment schedule. Each individual was imaged every minute for 10 minutes before any treatment and during the last 30 minutes of the diamide and DTT treatments (grey areas in the top bar).

(**b–d**) Fluorescence intensities and ratios for nine individuals in which the sensor was first maximally oxidized and then maximally reduced by diamide and DTT treatments, respectively. Panel b shows the ratio $R_{410/470}$ of the fluorescence intensities upon excitation with 410 nm (panel c) and 470 nm (panel d).

(**e–f**) From the $R_{410/470}$ and I_{470} time courses in panels b and d, respectively, we determined the three parameters required to relate the fluorescence ratio $R_{410/470}$ to the fraction of roGFP1_R12 molecules with a disulfide bond, OxD_{roGFP} : (i) R_{ox}, the value of $R_{410/470}$ when the sensor is fully oxidized; (ii) R_{red}, the value of $R_{410/470}$ when the sensor is fully reduced; (iii) $\alpha = I_{470(ox)} / I_{470(red)}$, the ratio of fluorescence intensities upon excitation with 470 nm when the sensor is fully oxidized and fully reduced. These three parameters enable the conversion of $R_{410/470}$ to OxD_{roGFP} (ref. [17]), shown in panel e: $OxD_{roGFP} = (R_{410/470} - R_{red})/[\alpha (R_{ox} - R_{410/470}) + (R_{410/470} - R_{red})]$. The parameters R_{ox} and R_{red} define the dynamic range of the sensor ($R_{ox} / R_{red} = 7.8$). Next, we used the Nernst equation to convert OxD_{roGFP} into E_{roGFP}, which is the half-cell reduction potential of the sensor redox couple. The parameter α shifts the relationship from $R_{410/470}$ to E_{roGFP} by a constant value. See Methods for additional considerations. Each of the nine time courses provides one set of three parameters (R_{ox}, R_{red} and α), yielding a particular OxD_{roGFP} vs $R_{410/470}$ (**e**) and E_{roGFP} vs $R_{410/470}$ (**f**) curve. These nine curves are shown in grey. The average value of each parameter ($R_{ox} = 5.207$, $R_{red} = 0.667$, and $\alpha = 0.171$) yields the curves shown in black that

were used throughout the paper to transform our fluorescent readout $R_{410/470}$ into a biophysically interpretable magnitude E_{roGFP}.

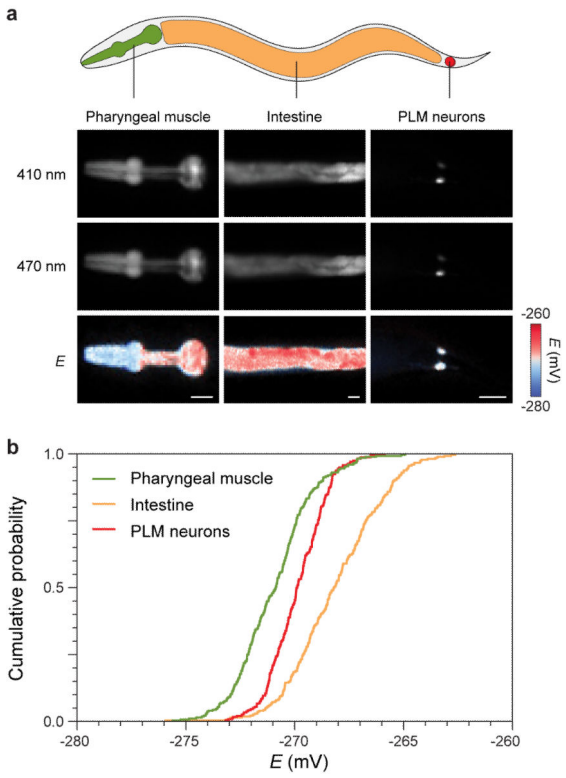

Figure 2. Tissue-specific differences in the sensor's redox potential

(**a**) Fluorescence images upon illumination with 410 nm and 470 nm for each tissue and pixel-by-pixel redox-potential visualization (scale bar equals 25 μm). These animals exhibit potentials close to those of their respective tissue averages.

(**b**) Cumulative distributions of the sensor's redox potential in the cytosol of pharyngeal muscles (green, 276 animals), PLM touch neurons (red, 239 animals) and intestine (orange, 276 animals), in day 2 adults. Differences in average potential between these tissues were significant ($p < 0.0001$ for all pair-wise comparisons, Tukey HSD test). For statistics see Supplementary Table 1.

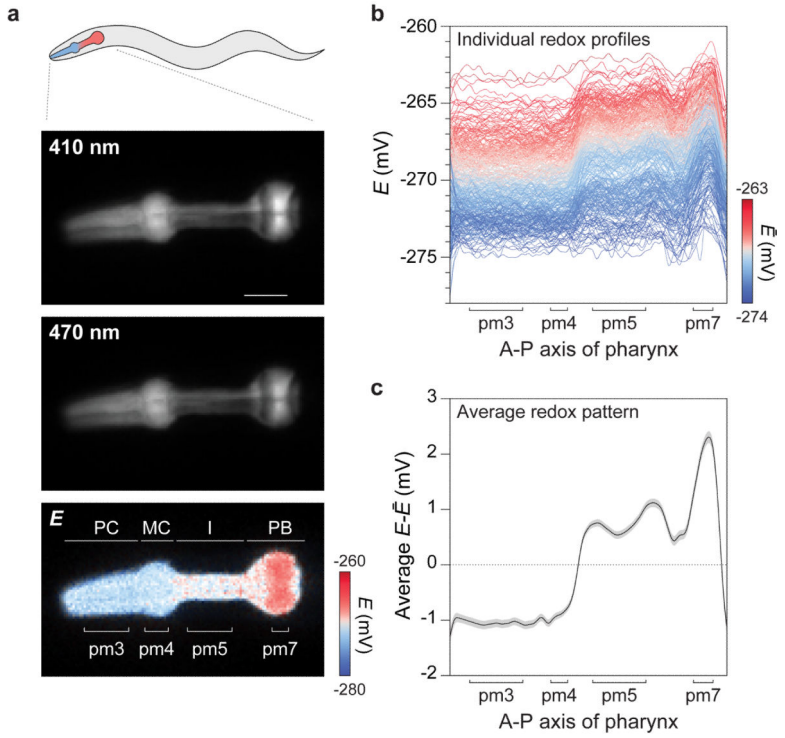

Figure 3. The sensor's redox potential is spatially patterned in the pharynx

(**a**) Fluorescence images upon illumination with 410 nm and 470 nm of an individual expressing roGFP1_R12 in the pharyngeal muscles (scale bar equals 25 μm). The bottom image is a color-coding of the pixel-by-pixel redox potential, derived from the ratio of the two images above. The annotations in the bottom image indicate the boundaries used to quantify the redox potential of specific muscles: pm3, pm4, pm5, and pm7, which are components of the anatomical regions known as the procorpus (PC), metacorpus (MC), isthmus (I), and posterior bulb (PB), respectively. This animal exhibits a redox potential close to the average for this tissue.

(**b**) This panel shows the redox profiles along the anterior-posterior axis of the pharynx of 394 wild-type animals. Each profile is represented as a continuous function in a B-spline basis that best fits the data points (see Supplementary Methods). The color of a profile is mapped to its average redox potential $\bar{E}$. Despite considerable variation in average potential across individuals, most share a distinct redox pattern relative to their tissue mean (panel c). An alternative representation is given in Supplementary Fig. 6. For statistics see Supplementary Table 2.

(**c**) Average pharyngeal redox pattern based on the 394 profiles shown in panel b. A pattern, as distinct from a profile, is defined as the departure of redox potential from the tissue average of an individual ($E - \bar{E}$). The overall pharyngeal pattern shown here is the average of all individual patterns. The shaded region represents the 95% point-wise confidence interval.

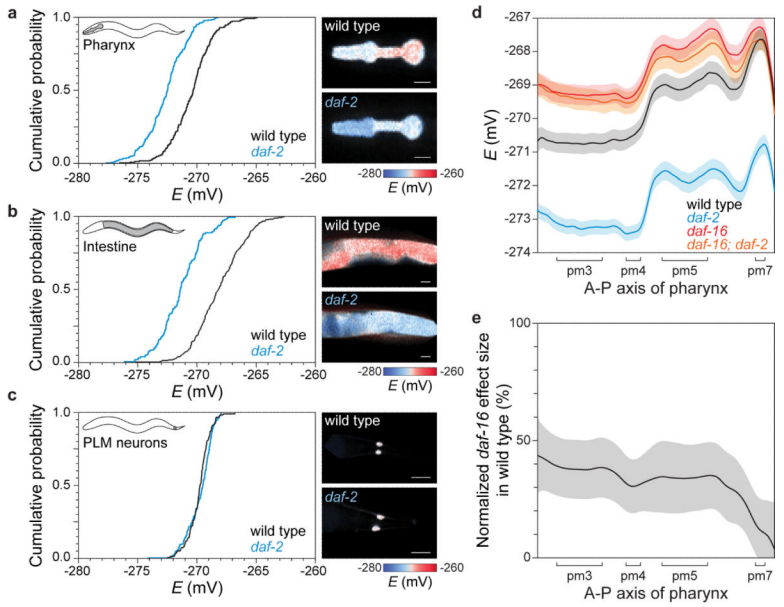

Figure 4. Insulin signaling regulates redox potential in different tissues and within a tissue

(**a–c**) Insulin signaling has tissue-specific effects on cytosolic redox potential. Cumulative distributions of cytosolic redox potentials in wild type and *daf-2(e1370)* mutants. The strong inhibition of insulin signaling in the *daf-2(e1370)* mutant causes a more reduced environment in the pharynx (a) and intestine (b), but does not affect the redox potential of the PLM touch neurons (c). Pixel-by-pixel redox potential images of representative animals, with potentials close to their respective tissue and genotype averages. Scale bar equals 25 μm. Populations sizes for wild-type and *daf-2(e1370)* were, respectively, 227 and 263 (pharynx), 276 and 151 (intestine), and 133 and 205 (PLM neurons). For statistics see Supplementary Table 3a.

(**d**) Insulin signaling has region-specific effects on the spatial redox profile in the pharynx. We compare the average redox potential along the anterior-posterior axis of the pharynx of wild type (black, 273 animals), *daf-2(e1370)* (blue, 225 animals), *daf-16(mu86)* (red, 224 animals), and the double mutant *daf-16(mu86); daf-2(e1370)* (orange, 209 animals). The latter two are statistically indistinguishable ($p > 0.05$, functional permutation t-test). Shaded areas represent 95% point-wise confidence intervals.

(**e**) Normalized *daf-16* effect size on the sensor's redox potential along the anterior-posterior axis of the pharynx. We quantify the effect size of *daf-16* on this phenotype using a functional version of categorical regression on genotype. This regression expresses the anterior-posterior redox profile in terms of the wild type profile plus effect terms derived from *daf-2* and *daf-16* single and double mutants (Supplementary Fig. 9b–c). In essence, the normalized effect of *daf-16* in wild type, is the difference between the black and the red curves divided by the difference between the blue and the orange curves. The latter difference is the maximal effect of *daf-16* controllable by *daf-2*. The panel shows that in most of the pharynx of wild type animals *daf-16* is kept around 40% of its maximal effect, decreasing to 0% in the posterior. The shaded area represents the 95% point-wise confidence interval.

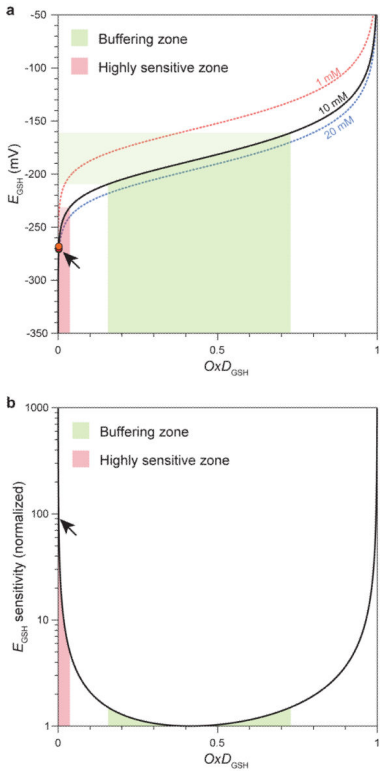

Figure 5. The cytosolic glutathione couple is not a buffer of redox potential

(**a**) The redox potential of glutathione thiol (GSH)/glutathione disulfide (GSSG) couple is given by the Nernst equation $E_{GSH} = E^{\circ\prime}_{GSH} - RT/(2F) \ln([GSH]^2/[GSSG])$, where R is the gas constant, F is the Faraday constant and T is the absolute temperature, here 295.15 °K. The midpoint (standard) potential $E^{\circ\prime}$ for the glutathione couple is −240 mV under biological standard conditions[35]. This equation can be rewritten in terms of total glutathione GSH_{tot} (equal to 2 [GSSG] + [GSH]) and the fraction of oxidized glutathione OxD_{GSH} (equal to 2 [GSSG] / GSH_{tot}), resulting in the expression $E_{GSH} = E^{\circ\prime}_{GSH} - RT/(2F) \ln [2\ GSH_{tot}\ (1 - OxD_{GSH})^2 / OxD_{GSH}]$. The panel shows the Nernst curves for GSH_{tot} = 1 mM, 10 mM, and 20 mM. A value of 10 mM is at the high end of physiological concentrations observed in other species[38]. Changes in the oxidation state of the glutathione couple will cause a large change in redox potential when the couple is in a highly sensitive (red) region of the curve and will cause a small change in redox potential when the couple is in a buffered (green) region of the curve. The colored circles indicate the intersection of the average cytosolic redox potentials we measured in pharyngeal muscles, intestine, and PLM touch neurons (Fig. 2) with the 10 mM GSH_{tot} curve.

(**b**) Normalized sensitivity of the redox potential E_{GSH} to changes in OxD_{GSH} (defined as the derivative of the Nernst curves shown in panel a, normalized to its minimum value). E_{GSH} sensitivity is independent of GSH_{tot}. Normalized sensitivity values below 1.5 indicate that the glutathione couple operates in a buffering regime ($0.157 < OxD_{GSH} < 0.729$, green), while values above 5 indicate a highly sensitive regime ($OxD_{GSH} < 0.037$, red; $OxD_{GSH} > 0.929$, not highlighted). The glutathione couple operates in a highly sensitive regime *in vivo* (for example, at $OxD_{GSH} = 0.0019$ associated with $E = -270$ mV, black arrow).

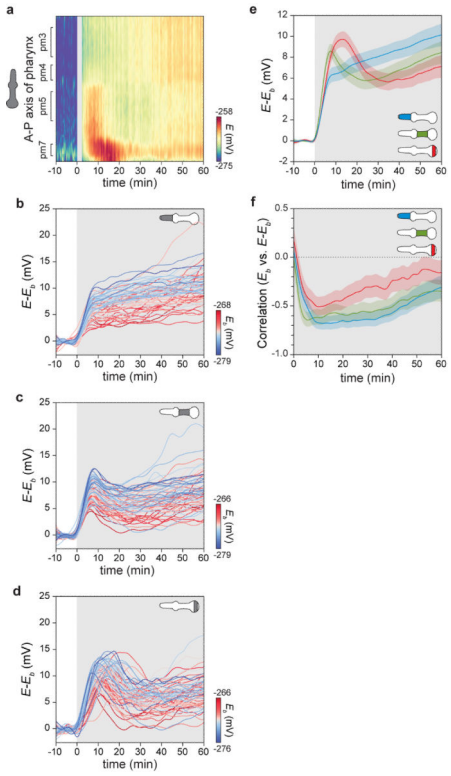

Figure 6. Variation in glutathione redox potential between individuals is caused by differences in glutathione oxidation

(**a**) Spatial and temporal response of the sensor's redox potential in an individual before and during treatment with with 5 mM *t*-BuOOH. Each column represents the redox profile of the individual along the anterior-posterior pharyngeal axis at a given time point. Each row is a time point at a given spatial location. Worms were imaged every 30 seconds. Oxidant exposure starts at $t = 0$ (gray background in panels b–f).

(**b–d**) The spatio-temporal response to 5 mM *t*-BuOOH treatment was recorded in 64 individuals. For each individual, we determined the responses of pm3, pm5 and pm7 (panels b, c, d, respectively). Each time series was baseline-corrected by subtracting its average potential prior to oxidant exposure. The resulting time series were converted into a continuous function using a spline basis (for the non-baseline corrected set see Supplementary Fig. 10; for the quality of the fit see Supplementary Fig. 11). The coloring encodes the average potential before oxidant exposure (E_b).

(**e**) Average response dynamics. The functionalized trajectories of redox potential in pm3 (blue), pm5 (green) and pm7 (red) were pooled and subjected to functional categorical regression[34] on the regions of origin (pm3, pm5, pm7). This procedure yields the average time-dependent response dynamics in each region. Shaded areas represent 68% point-wise confidence intervals.

(**f**) This panel shows, for each muscle, the Pearson correlation between the individual redox baselines prior to perturbation and the baseline-corrected response after perturbation. The strong initial negative correlation implies that we mostly see different baseline potentials on the same Nernst curve rather than different curves corresponding to distinct values of total glutathione (see text for details). The subsequent correlation decay indicates that an adaptive

response to perturbation is becoming prominent. Shaded areas represent 68% point-wise confidence intervals.

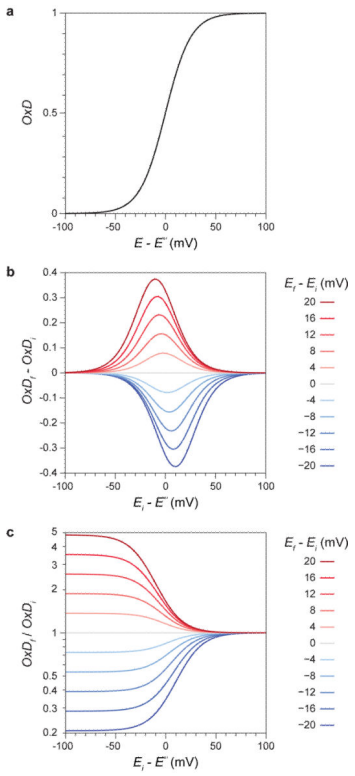

Figure 7. Analysis of the sensitivity of protein oxidation to changes in glutathione redox potential

(**a**) Relationship between redox potential and protein oxidation. The Nernst equation relates the redox potential *E* to the fraction oxidized *OxD* of a redox couple. This relation depends on the couple's midpoint potential *E*°' (which quantifies the affinity for electrons of the oxidized species). The panel depicts the Nernst curve relative to the midpoint *E*°', i.e. *OxD* vs $E - E°'$, with $OxD = 1/(\exp[-(E - E°')2F/RT] + 1)$ and $T = 295.15$ °K. See Supplementary Note 2 for additional considerations.

(**b**) Effect of a redox-potential change on absolute protein oxidation levels. The calculation of the change in *OxD* upon a change in potential from $E_i - E°'$ to $E_f - E°'$ (that is, $\Delta E = E_f - E_i$), depends on whether the relevant biochemical quantity is the ensuing difference $OxD_f - OxD_i$ (this panel) or fold-change OxD_f/OxD_i (panel c). The abscissa shows the initial redox potential E_i of a protein relative to its midpoint *E*°'.The potential E_i entails a certain fraction of oxidized protein OxD_i. When the potential changes from E_i to E_f, the fraction of protein oxidized changes accordingly from OxD_i to OxD_f. This change is reported by the various curves, one for each potential difference $\Delta E = E_f - E_i$ shown in the legend.

(**c**) Effect of a redox-potential change on relative protein oxidation levels. As in panel b, but the change of interest is now the ratio of OxD_f at E_f to OxD_i at E_i. Note that this is a log-linear plot. The largest fold-change occurs when the initial *OxD* is as small as possible, since then even the smallest change in *OxD* results in a dramatic fold-change. This occurs at very negative E_i, far to the left of the midpoint. The fold-change will be very large (very small) for positive (negative) ΔE. If the protein couple is far to the right of the midpoint, *OxD* is near maximal and only small changes can occur, resulting in a fold-change close to 1.

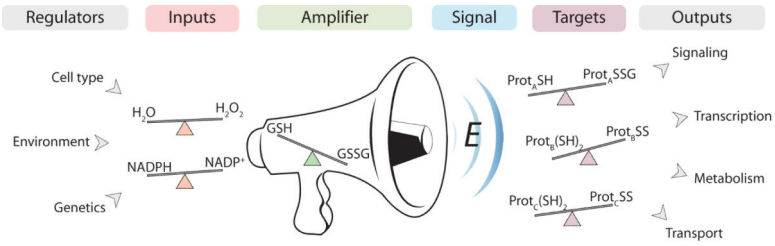

Figure 8. Model for redox control of protein function in the cytosol

The cytosolic glutathione couple is positioned *in vivo* to sensitively amplify redox events affecting its oxidation state, via its redox potential *E*. This signal, in turn, controls the activity of target proteins with embedded cysteine residues by affecting their thiol-disulfide balance. The resulting changes in activity may impact the cellular processes affected by these proteins.